

Spin Relaxometry with Solid-State Defects: Theory, Platforms, and Applications

Ruotian Gong ,¹ Alex L. Melendez ,² Guanghui He ,^{1,2} Zhongyuan Liu ,¹ Chong Zu ,^{1,*} and Huan Zhao ,^{2,†}

¹*Department of Physics, Washington University in St. Louis, St. Louis, MO 63130, USA.*

²*Center for Nanophase Materials Sciences, Oak Ridge National Laboratory, Oak Ridge, TN 37831, USA.*

Spin relaxometry using solid-state spin defects, such as the diamond nitrogen-vacancy (NV) center, probes dynamical processes by measuring how environmental fluctuations enhance the spin relaxation rate. In the weak-coupling limit, relaxation rates sample the transverse magnetic-noise power spectral density through a sensor-specific filter function, turning the defect into a local, frequency-selective noise spectrometer. This review bridges theory and experiment, clarifying how measured relaxation rates map onto noise spectra and how near-field geometry shapes the response. We highlight representative applications across condensed-matter physics, chemical and biological sensing, and relaxometry-based magnetic-resonance spectroscopy. We conclude with emerging opportunities and key challenges.

1. EXECUTIVE MAP

This review is organized around a simple translation: *dynamics in a nearby system* \rightarrow *magnetic-field fluctuations at the sensor* \rightarrow *a change in the sensor's spin-relaxation time*. We use the NV center as the primary sensor throughout, as it is the most established solid-state platform for relaxometry. The key message is that relaxometry provides a local, spectrally selective probe of the environmental magnetic-noise power spectral density (PSD) $S_B(\omega)$.

- **Relaxometry measures fluctuations, not fields.** In contrast to magnetometry (which measures a quasi-static stray field), relaxometry detects time-dependent magnetic noise, i.e., the PSD as a function of frequency, $S_B(\omega)$. [1, 2].
- **Spin relaxation time, T_1 , is a built-in noise spectrometer at the NV transition frequency.** In the weak-coupling regime, the longitudinal relaxation rate is proportional to transverse magnetic noise evaluated at the sensor transition frequency,

$$\Gamma_1 \equiv \frac{1}{T_1} \propto S_{B_\perp}(\omega_{\text{NV}}), \quad (1)$$

where ω_{NV} is tunable by an applied magnetic field [1, 3].

- **Different decay constants probe different frequency bands.** Roughly: T_2^* (Ramsey) probes near-DC noise, T_2 (echo/dynamical decoupling) probes kHz–MHz bands set by pulse spacing, $T_{1\rho}$ (spin-lock) probes noise near the Rabi frequency, and T_1 probes near ω_{NV} (typically MHz–GHz depending on field) [1, 2, 4].
- **Rates add, so baselines are not optional.** The measured relaxation rate is typically well-described by

$$\Gamma_{\text{total}} = \Gamma_{\text{intrinsic}} + \Gamma_{\text{sample}} + \Gamma_{\text{tech}}, \quad (2)$$

where Γ_{tech} denotes technical and optical artifacts (e.g., heating, charge conversion, surface noise). Controls (reference regions, height dependence, before/after comparisons) are essential for attributing Γ_{sample} to physics [5–8].

- **Cross-relaxometry turns $T_1(B)$ into a spectrum.** Sweeping the static field tunes $\omega_{\text{NV}}(B)$ across target resonances. Resonant coupling produces dips/peaks in $T_1(B)$ that fingerprint electron-spin or nuclear-spin transitions without directly driving the sample with microwaves [9–12].
- **Geometry and distance filter what you see.** The NV senses stray-field noise outside the sample; the NV–sample distance h acts as a near-field spatial filter that suppresses fluctuations with wavelength $\ll h$. Quantitative interpretation therefore requires modeling not only the material response (spin/current correlations) but also the field propagator from the sample to the NV [2, 13–15].
- **Relaxometry is versatile because many systems generate magnetic noise.** Thermally populated magnons in magnets, fluctuating currents in conductors (Johnson noise), vortex motion and quasiparticles in superconductors, and paramagnetic species in chemistry/biology can all produce measurable changes in Γ_1 [13, 14, 16–19].

The remainder of this review provides a practical, quantitative roadmap for implementing spin relaxometry, and surveys representative applications of the technique.

2. INTRODUCTION

NV quantum sensing often proceeds by mapping a magnetic signal onto a *frequency shift* (optically detected magnetic resonance, or ODMR) or a *phase* (Ramsey/echo). Relaxometry uses a different observable: the *rate* at which the spin loses polarization or coherence due

to coupling to time-dependent environmental fields. In its simplest form, a T_1 measurement initializes the NV into a known population state, waits a variable delay τ , and reads out the remaining polarization optically. The measured fluorescence signal is then fit to an exponential (or sum of exponentials) to extract an effective T_1 .

Two features make relaxometry uniquely useful. First, it is naturally a *noise spectroscopy* tool: in the weak-coupling regime, the relaxation rate is set by the environmental PSD at specific frequencies determined by the sensor transition and the applied control. Second, it is inherently *local*: the NV samples the near field of the environment, so the signal can be strongly distance dependent and spatially resolvable in scanning and wide-field geometries.

In practice, relaxometry is used in two complementary modes: (i) **Imaging at fixed field**: measure $\Gamma_1(\mathbf{r})$ to map spatial variations in noise (e.g., local defects, domain walls, current paths). (ii) **Spectroscopy via tuning**: sweep the static magnetic field to tune $\omega_{\text{NV}}(B)$ and obtain $\Gamma_1(B)$ (or $T_1(B)$), which reveals resonant modes and cross-relaxation features [9, 10, 12].

A key interpretational point is that the NV does not “directly” measure a material parameter. Rather, it measures a decay constant that must be connected to the underlying degrees of freedom through a model of (a) the relevant correlations in the sample (spins, currents, vortices, etc.) and (b) the geometry-dependent mapping from those sources to the magnetic field at the NV location [1, 2]. Throughout this review we emphasize practical strategies—baseline subtraction, height dependence, field dependence, and independent knobs (temperature, drive power, device configuration)—that help make this inference robust.

The negatively charged NV center (NV^-) is an $S = 1$ electronic spin defect in diamond with a ground-state zero-field splitting $D \approx 2.87 \text{ GHz}$ between the $m_s = 0$ and $m_s = \pm 1$ sublevels. Green illumination optically pumps the spin into $m_s = 0$ and enables spin-state-dependent fluorescence readout [2, 4, 20–22]. For relaxometry, two properties are central. The first one is spectral selectivity and tunability: environmental magnetic noise is generally broadband in frequency, but the NV spin only relaxes efficiently when noise has spectral weight near its transition frequencies. In this sense, the NV spin acts as a narrow-band filter function that picks out the component of the noise spectrum resonant with its spin transition energy. An applied magnetic field then tunes the transition frequencies $\omega_{0 \leftrightarrow \pm 1}(B)$, allowing the sensor to “scan” different parts of the environmental noise spectrum by changing B , and enabling cross-relaxometry when ω_{NV} matches a target transition [9–11]. The second property is near-field coupling, which emphasizes that relaxometry is a local probe. To achieve best sensitivity, near-surface NV centers can be positioned within $\sim 10 \text{ nm}$ of a sample, making the dipolar coupling to nearby spins

and currents strong enough that weak magnetic noise can measurably modify Γ_1 [5–7].

In most room-temperature relaxometry experiments, the NV is treated as an effective two-level system (e.g., $\{|0\rangle, |1\rangle\}$) whose population relaxation is driven primarily by transverse magnetic noise. However, there are important regimes where this simplification fails or requires care. Strain and off-axis magnetic fields can mix the $m_s = \pm 1$ manifold, and hyperfine interactions split each transition into multiple lines. Near level anticrossings (especially near the ground-state level anticrossing), mixing with nuclear spins can strongly modify relaxation pathways and enable nuclear-frequency cross-relaxation [10, 11, 23, 24].

We aim to serve two audiences at once: (i) readers who want a practical experimental playbook, and (ii) readers who want a clear, quantitative link between a measured decay constant and a physical noise source. In the remainder of this review, we first introduce the main spin-relaxometry platforms, covering different quantum sensors and experimental hardware architectures. We then develop the theoretical framework for spin relaxation experiments, linking changes in the relaxation rate to the underlying magnetic-noise spectrum and highlighting the role of spectral filter functions and cross-relaxometry [1, 2, 4]. Next, we discuss applications of spin relaxometry in both physical science and life science, emphasizing recent advances in quantum materials, transport, superconductivity, nano-/micro-NMR, and biological/chemical sensing. Finally, we conclude with an outlook on both challenges and future opportunities, including quantitative inversion of $S(\omega)$, standardization and uncertainty quantification, and prospects for new sensor materials and device architectures.

3. SPIN-DEFECT RELAXOMETRY PLATFORMS

Solid-state spin defects are point defects in crystals that possess a paramagnetic spin state and can be interrogated optically. Crucially, many solid-state defects function at room temperature and can convert magnetic noise into optical fluorescence signals (Fig. 1a), enabling highly sensitive, non-invasive measurements with nanometer-scale resolution. Below, we briefly survey the main solid-state spin-defect platforms used for relaxometry, namely diamond NV centers, spin defects in hexagonal boron nitride (hBN), defects in silicon carbide (SiC), and emerging new platforms, emphasizing what each enables experimentally and what limitations typically dominate.

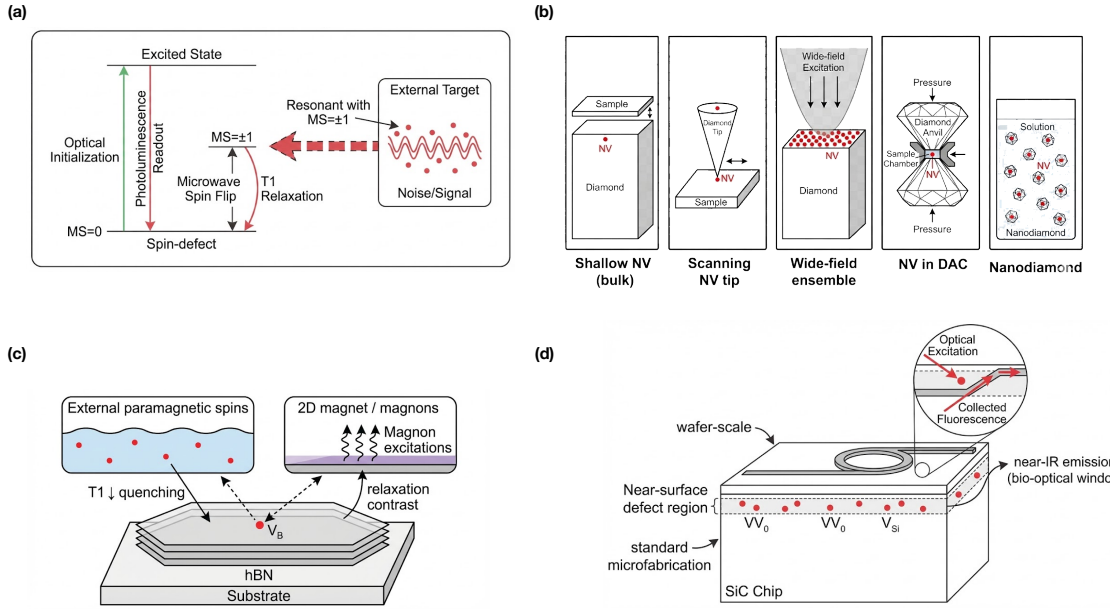


FIG. 1. Experimental platforms for spin relaxometry. (a) Principle of spin relaxometry as frequency-selective noise detection: Optical pumping initializes the defect spin (e.g., NV) and photoluminescence readout monitors its population dynamics. Longitudinal relaxation (T_1) is enhanced by transverse magnetic noise with spectral weight resonant with the spin transition (tunable via bias field and, when used, microwave control), enabling spectroscopy of external targets through resonant energy exchange with the environment. (b) NV-based spin relaxometry modalities and hardware geometries: Schematic illustrations of (from left to right) shallow near-surface NV centers in bulk diamond, scanning NV tips, wide-field NV ensembles, NV centers under high pressure in a diamond anvil cell (DAC), and fluorescent nanodiamonds in solution for relaxometric sensing in diverse environments. (c) Hexagonal boron nitride (hBN), as a two-dimensional spin-relaxometry platform, enables intrinsically small sensor–environment standoff distances, which is particularly advantageous in van der Waals heterostructures where hBN can be stacked directly with other 2D materials that host spin and charge noise. (d) Silicon carbide (SiC) is a promising host for chip-integrated spin relaxometry, leveraging wafer-scale processing, mature device fabrication, and defect spins that are compatible with on-chip photonic and electronic integration.

3.1 Diamond NV Centers

The NV center in diamond is the most established spin-defect platform for relaxometry and, more broadly, for nanoscale sensing. It consists of a substitutional nitrogen atom adjacent to a carbon vacancy in the diamond lattice. This defect has a spin-1 triplet ground state that can be polarized and read out optically at room temperature. Being hosted in diamond's robust lattice, NV centers offer robust optical initialization and readout at room temperature, well-developed materials processing (implantation, delta-doping, surface termination), and long spin coherence and relaxation times [4, 20, 22]. In the context of relaxometry, NV centers can sensitively convert fluctuation magnetic fields into changes in their fluorescence, effectively acting as nanoscale T_1 sensors. The NV-based relaxometry was first demonstrated in 2013, when

researchers showed that an NV's T_1 relaxes faster in the presence of nearby paramagnetic ions, such as Gd^{3+} [25]. Since then, NV relaxometry has been applied widely, and a practical advantage of diamond NVs is the diversity of sensor geometries (Fig. 1b):

- **Single near-surface NVs in bulk diamond:** maximize spatial resolution and coupling to local fluctuators, but can be limited by surface-related magnetic noise and charge instability [5–7].
- **Scanning NV probes (diamond tips):** enable controlled NV-sample distance and sub-diffraction-limit imaging, at the cost of slower acquisition and added drift/stability constraints [21, 26].
- **Wide-field NV ensembles (near-surface layers):** enable parallel relaxometry probing of over

large fields of view (including pixel-wise T_1 maps), with resolution set by diffraction, sensor depth, and pixel size [1, 27].

- **Diamond anvil cell (DAC) implementations:** NV layers integrated into/onto anvils enable quantum sensing under extreme pressures while retaining optical access; this opens relaxometry-compatible pathways to probe pressure-tuned magnetism and superconductivity in micron-scale samples [28–32].
- **Nanodiamonds:** provide straightforward integration into liquids and cells, but typically introduce larger inhomogeneity and more complex surface chemistry that can broaden T_1 distributions and add platform-specific backgrounds [22, 33].

Despite its success, the NV platform has some limitations. One challenge is the need to position NV centers close to the sample of interest (typically within 10 nm of the diamond surface) to sense external spins. However, creating such shallow NVs often degrades their spin properties due to surface-induced noise, which can shorten the coherence and relaxation times (i.e. reducing sensitivity) [5–7]. Additionally, while diamond is an excellent host, it is a three-dimensional crystal, which means that integrating diamond sensors with other nanoscale materials or devices can be non-trivial. Nonetheless, the diamond NV center remains the gold standard for solid-state relaxometry, offering a proven combination of sensitivity, room-temperature operation, and nanoscale resolution.

3.2 hBN defects

The surface-noise and charge-instability penalties that often accompany shallow NV centers motivate platforms where the spin is intrinsically at an interface. Hexagonal boron nitride (hBN) is a wide band gap (~ 6 eV) van der Waals material that can be exfoliated to the few-layer limit and integrated into heterostructures, enabling ultra-small sensor-sample standoff without the need for near-surface defect engineering in a 3D crystal [34]. The best-established hBN spin defect is the negatively charged boron vacancy V_B^- , which exhibits room-temperature ODMR and coherent control [35–40]. The V_B^- center consists of a missing boron atom in the lattice, where the negatively charged state results in a spin-1 system highly similar to NV center. Beyond boron vacancies, other carbon-related defects in hBN have been reported to show ODMR as well (e.g., defects involving carbon substitution in the lattice) [41, 42]. While their structures are still being actively studied, these additional spin defects with brighter emission indicate that hBN may host a family of optically addressable spins with potentially diverse sensing properties [43, 44].

Though still a young platform, hBN spin defects have already demonstrated the core capability for relaxometry. A recent breakthrough showed that V_B^- can detect external paramagnetic spins T_1 quenching under ambient conditions [45]. Another exciting application of hBN defects is in probing magnetic phenomena in 2D heterostructures and devices since hBN layers can be integrated into heterostructures (Fig. 1c). V_B^- centers have been used to sense spin wave (magnon) excitations in a magnetic layer through changes in the relaxation rate and resonance signals [46, 47]. On the other hand, hBN spin defects face several challenges as an emerging platform. The spin properties of hBN defects currently lags behind NV centers in quality, and the sensitivity also suffers from shorter intrinsic relaxation times. The V_B^- centers are also much dimmer than NVs, which reduces photon-limited readout fidelity and often forces the use of ensembles or longer averaging times for relaxometry measurements. Despite these challenges, the rapid progress and these early studies position hBN as a flexible 2D quantum sensor that complements the NV center by offering closer sample coupling and new integration possibilities.

3.3 SiC and other emerging defects

Like diamond and hBN, Silicon carbide (SiC) is a wide-bandgap semiconductor that hosts several important spin defects. Two well-known spin-active centers in SiC are the neutral divacancy ($VSiV_C^0$, often abbreviated as VV_0) and V_{Si}^- the silicon vacancy [48–51]. The divacancy in 4H-SiC consists of an adjacent carbon vacancy and silicon vacancy pair; it is isoelectronic to the NV and V_B^- (an spin-1 triplet with optical transitions that enable spin polarization and readout). The negatively charged silicon vacancy (often at the so-called V2 site in 4H-SiC) is a spin-3/2 system that also exhibits ODMR at room temperature. A major appeal of SiC as a host is the availability of high-quality, wafer-scale material and established microfabrication techniques. In other words, SiC defects can be integrated into devices (e.g. nanophotonic cavities, electrical circuits) using standard semiconductor processing (Fig. 1d). Both VV_0 and V_{Si}^- centers have demonstrated long spin coherence times (up to milliseconds) in isotope-purified SiC and can be engineered at specific sites or depths via ion implantation [51, 52]. Although research on SiC defects initially focused on quantum communication and computing, there is growing interest in their use for relaxometry-based sensing. Recent work has pushed SiC divacancy qubits toward practical relaxometry: near-surface defects have been used for T_1 -based detection of surface paramagnetic species, highlighting SiC as a promising, device-compatible alternative for relaxometry [53]. SiC spin defect offers clear advantages like compatibility with existing tech and bio-

optical windows, but requires continued improvements in defect engineering and surface science to fully match the sensitivity of conventional counterparts.

Beyond NV, hBN, and SiC, a broader landscape of optically addressable spins is under active development; however, most remain at the level of sensing demonstrations rather than established, quantitative nanoscale T_1 relaxometry. For example, rare-earth-ion-doped crystals (e.g., Eu/Pr/Er in oxide hosts) offer exceptionally narrow optical transitions and long-lived spin states at cryogenic temperatures, which is why they are widely used for quantum memories and coherent spectroscopy [54–56]. However, most sensing demonstrations to date rely on spectral shifts / coherent optical spectroscopy rather than relaxometry, and the need for cryogenic operation remains a major practical constraint. Another prospective 2D host is the family of transition-metal dichalcogenides (e.g., WS₂, WSe₂, MoTe₂), where extensive defect engineering and single-photon-emitter (SPE) work already exists, including SPEs operating at technologically relevant telecom wavelengths [57–59]. Several first-principles studies have specifically proposed spin-triplet defect candidates in monolayer TMDs (e.g., antisite defects, or transition-metal substitutions at chalcogen sites) with optical transitions that could be compatible with spin readout [60–62]. At present, however, these remain largely computational blueprints, and robust room-temperature ODMR and quantitative T_1 -relaxometry demonstrations in TMD defects are still much less established.

4. THEORY OF SPIN RELAXOMETRY

The goal of this section is to make explicit how measured relaxation rates (e.g., T_1 , $T_{1\rho}$) connect to the environmental magnetic-noise spectral density $S_B(\omega)$. We first write down a minimal Hamiltonian for the NV, then use a Bloch–Redfield / Fermi–Golden-Rule picture to relate Γ_1 to $S_{B_\perp}(\omega_{\text{NV}})$, and finally place T_1 within the broader filter-function framework that also covers T_2^* , T_2 , and $T_{1\rho}$ [1, 2, 4]. Throughout this review we focus primarily on longitudinal (T_1) relaxometry, which provides a particularly direct route to nanoscale noise spectroscopy and is widely used in current experiments. For completeness, this theory section briefly summarizes complementary “relaxometric” and coherence-based modalities that access different spectral windows. We close with a brief discussion of cross-relaxometry as resonant spectroscopy [9–12].

4.1 NV spin Hamiltonian and transition frequencies

A minimal Hamiltonian for the NV[−] ground state is

$$\mathcal{H} \approx DS_z^2 + \gamma_e \mathbf{B} \cdot \mathbf{S} + \mathcal{H}_{\text{hf}} + \mathcal{H}_{\text{strain}} + \mathcal{H}_{\text{noise}}, \quad (3)$$

where D is the zero-field splitting, $\gamma_e \approx 28 \text{ GHz/T}$ is the electron gyromagnetic ratio, \mathcal{H}_{hf} includes hyperfine interactions with the host ¹⁴N/¹⁵N and nearby ¹³C spins, $\mathcal{H}_{\text{strain}}$ describes strain and electric-field-induced splitting and mixing of the $m_s = \pm 1$ manifold, and $\mathcal{H}_{\text{noise}}$ represents coupling to time-dependent magnetic fields generated by the environment [2, 20, 21]. The spin operator $\mathbf{S} = (S_x, S_y, S_z)$ acts on the spin-1 triplet $\{|+1\rangle, |0\rangle, |-1\rangle\}$.

For many relaxometry experiments, one works in a field regime where the NV quantization axis is set by the crystal axis, and the Zeeman term is dominated by the projection B_{\parallel} along this axis. Neglecting strain and off-axis fields for the moment, the eigenstates remain close to the m_s basis and the transition frequencies between $|0\rangle$ and $|\pm 1\rangle$ are approximately

$$\omega_{0 \leftrightarrow \pm 1}(B_{\parallel}) \approx 2\pi(D \pm \gamma_e B_{\parallel}). \quad (4)$$

Strain and off-axis fields B_{\perp} mix the $m_s = \pm 1$ states and can produce avoided crossings, especially near points where $\gamma_e B_{\parallel}$ cancels parts of the zero-field splitting. Hyperfine couplings further split each electronic transition into multiple hyperfine lines, typically separated by a few MHz for the host nitrogen and for nearby strongly coupled ¹³C spins [2, 20].

In practice, relaxometry often treats the NV as an effective two-level system: either $\{|0\rangle, |-1\rangle\}$ or $\{|0\rangle, |+1\rangle\}$. This is justified when one transition is spectrally isolated and the other is far detuned; the neglected level then only contributes weakly via second-order processes [2, 4]. However, near level anticrossings (e.g., the ground-state level anticrossing near $B_{\parallel} \sim 102 \text{ mT}$), all three levels and coupled nuclear spins can participate, and a full spin-1 (or spin-1 + nuclear spin) treatment is necessary to interpret T_1 and cross-relaxation features [10, 11].

4.2 T_1 relaxometry as magnetic-noise spectroscopy

We now outline how longitudinal relaxation arises from transverse magnetic noise. For simplicity, consider an effective two-level system formed by $|0\rangle$ and $|1\rangle$, where $|1\rangle$ denotes one of the $m_s = \pm 1$ states. We separate the Hamiltonian into a static part and a noisy perturbation,

$$\mathcal{H}_0 = \frac{\hbar\omega_{\text{NV}}}{2} \sigma_z, \quad (5)$$

$$\mathcal{V}(t) = -\hbar\gamma_e [B_x(t)S_x + B_y(t)S_y], \quad (6)$$

where σ_z acts in the $\{|0\rangle, |1\rangle\}$ subspace, and $B_x(t), B_y(t)$ are stochastic, zero-mean magnetic fields transverse to

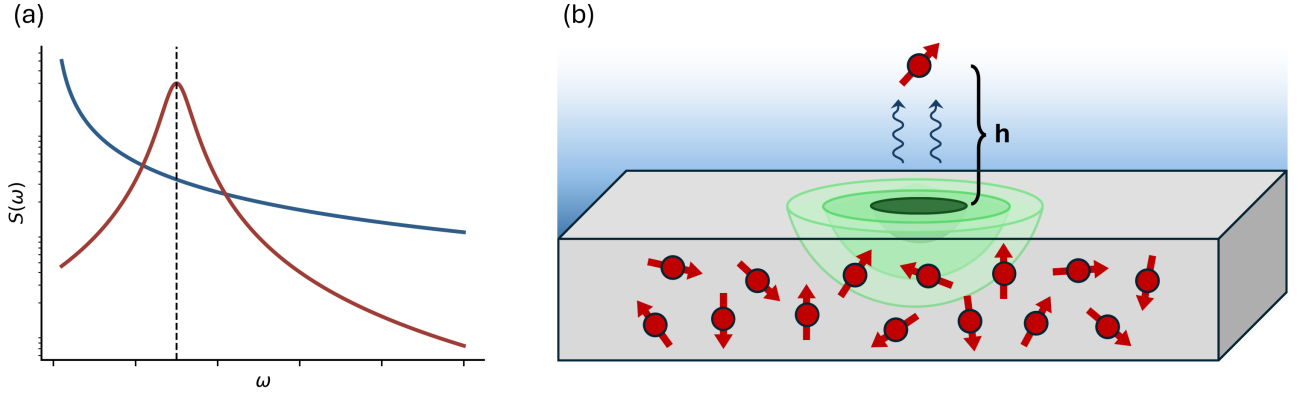


FIG. 2. (a) Schematic of overlap between power spectral density of sample (blue) with that of the spin defect (red). Center (ODMR) frequency of spin defect is represented by the vertical gray dashed line. (b) Schematic of a single spin sensor experiencing magnetic field fluctuations (blue gradient/squiggly arrows) above a sample of fluctuating spins. The sensor spin is sensitive to a sample volume illustrated by the concentric green hemispheres, with stronger coupling to spins near the center (dark green) and falling off as r^{-6} . The distance h sets the spatial resolution of the sensor.

the quantization axis (we ignore longitudinal noise here, which primarily affects dephasing).

Within Bloch–Redfield theory or Fermi’s Golden Rule, the upward ($0 \rightarrow 1$) and downward ($1 \rightarrow 0$) transition rates are proportional to the noise power at the transition frequency [1, 2]:

$$\Gamma_{0 \rightarrow 1} \propto S_{B_\perp}(-\omega_{\text{NV}}), \quad (7)$$

$$\Gamma_{1 \rightarrow 0} \propto S_{B_\perp}(+\omega_{\text{NV}}), \quad (8)$$

where we have defined the transverse noise power spectral density (PSD)

$$S_{B_\perp}(\omega) = \int_{-\infty}^{\infty} dt e^{i\omega t} \langle B_\perp(t) B_\perp(0) \rangle, \quad (9)$$

and B_\perp denotes the appropriate combination of B_x and B_y that couples the two levels. For classical, high-temperature noise, the PSD is effectively symmetric in frequency, so $S_{B_\perp}(\omega_{\text{NV}}) \approx S_{B_\perp}(-\omega_{\text{NV}})$ [2].

The total longitudinal relaxation rate is then

$$\Gamma_1 = \Gamma_{0 \rightarrow 1} + \Gamma_{1 \rightarrow 0} \approx \frac{\gamma_e^2}{2} S_{B_\perp}(\omega_{\text{NV}}), \quad (10)$$

up to angular factors and matrix elements of S_x, S_y between $|0\rangle$ and $|1\rangle$ [1, 3]. This is the crucial result: T_1 is inversely proportional to the magnetic-noise PSD at the sensor transition frequency [1, 3] (Fig. 2a).

In this picture, only transverse noise contributes to Γ_1 : longitudinal noise (along the quantization axis) does not induce spin flips in lowest order and instead leads to dephasing. The relaxation rate is also proportional to the square of the coupling (here $\gamma_e B_\perp$), which makes shallow NVs and strong coupling geometries particularly valuable, but also increases sensitivity to unwanted surface and technical noise [5–7]. Finally, the proportionality constant depends on matrix elements and on whether

the noise is classical or quantum. For many room-temperature applications, the high-temperature approximation is valid and the classical expression above suffices; near cryogenic conditions or for high-frequency modes one may need to keep the full quantum detailed-balance factors [2, 19].

In experiments, one measures the fluorescence contrast as a function of wait time τ and fits it to an exponential (or sum of exponentials),

$$C(\tau) \sim C_0 \exp(-\Gamma_1 \tau) + C_\infty, \quad (11)$$

extracting the effective Γ_1 [1, 3]. The statement that T_1 “measures” $S_{B_\perp}(\omega_{\text{NV}})$ should be understood as: given a model for the coupling between sample degrees of freedom and $B_\perp(t)$ at the NV location, the measured Γ_1 constrains the amplitude and correlation time of those degrees of freedom at frequency ω_{NV} [1, 13, 14].

4.3 Beyond T_1 : T_2^* , T_2 , and $T_{1\rho}$

The connection between relaxation/decoherence and noise is not unique to T_1 ; it is a special case of a more general filter-function framework. For pure dephasing under a control sequence (Ramsey, echo, dynamical decoupling), the coherence function typically takes the form

$$W(\tau) = \exp[-\chi(\tau)], \quad (12)$$

$$\chi(\tau) = \frac{\gamma_e^2}{\pi} \int_0^{\infty} d\omega S_{B_\parallel}(\omega) |F(\omega, \tau)|^2, \quad (13)$$

where $S_{B_\parallel}(\omega)$ is the PSD of longitudinal (dephasing) noise and $F(\omega, \tau)$ is a filter function determined solely by the control sequence [2, 4]. Different sequences correspond to different $F(\omega, \tau)$ and thus to different frequency windows of sensitivity.

Although T_1 arises from transverse noise and involves population relaxation rather than pure dephasing, it can be viewed as another frequency-selective probe: it predominantly samples transverse noise in the 0.01 to 10 GHz frequency, with an effective bandwidth set by the homogeneous linewidth of the transition [1, 2]. By analogy, one can qualitatively classify the main NV decay constants as follows. Ramsey dephasing (T_2^*) is most sensitive to quasi-static and low-frequency noise, since the corresponding filter function is peaked near $\omega \approx 0$ and slow fluctuations and inhomogeneous fields dominate. Hahn echo and dynamical decoupling (T_2) suppress quasi-static contributions and become sensitive to noise near frequencies set by the inverse evolution time; multi-pulse sequences effectively create a comb of passbands that can extend sensitivity into the kHz–MHz regime [2, 4]. Spin-lock relaxometry ($T_{1\rho}$) probes noise near the Rabi frequency Ω in the rotating frame, typically in the 10 kHz to 10 MHz range depending on available microwave power, and thus bridges the gap between echo-based probes of low-frequency noise and T_1 -based probes at ω_{NV} [1, 5]. Finally, longitudinal relaxation (T_1) probes transverse noise near ω_{NV} , providing access to higher-frequency dynamics such as magnons, Johnson noise, and superconducting fluctuations [1, 13, 14, 19].

A practical takeaway is that these methods are not competitors but complementary spectral windows on the same underlying noise. By combining T_2^* , T_2 , $T_{1\rho}$, and T_1 measurements—possibly at multiple NV depths and magnetic fields—one can reconstruct $S_B(\omega)$ over many orders of magnitude in frequency and attribute different parts of the spectrum to different physical mechanisms (surface spins, phonons, magnons, currents, etc.) [1, 2, 15].

4.4 Relating magnetic noise to material response

To extract material parameters from relaxometry, one must connect the local magnetic noise $S_B(\omega)$ at the NV position to the underlying degrees of freedom in the sample. This connection typically has two pieces:

1. a material response, described by current or spin correlation functions (or equivalently, by dynamical susceptibilities);
2. a geometrical propagator, describing how these currents or spins generate magnetic fields at the NV location.

For spin systems (e.g., magnets, paramagnets), one often starts from the spin–spin correlation function or the imaginary part of the dynamical susceptibility $\chi''(\mathbf{q}, \omega)$. The fluctuation–dissipation theorem relates the Fourier

transform of magnetization fluctuations to χ'' :

$$S_{M_\alpha M_\beta}(\mathbf{q}, \omega) = \frac{2\hbar}{1 - e^{-\hbar\omega/k_B T}} \chi''_{\alpha\beta}(\mathbf{q}, \omega), \quad (14)$$

and $S_B(\omega)$ is then obtained by propagating these magnetization fluctuations through appropriate magnetostatic Green’s functions [2, 14, 15]. The NV does not couple directly to M in momentum space, but to the stray magnetic field generated by $M(\mathbf{r}, t)$, which introduces a q -dependent kernel $G(\mathbf{q}, h)$ that filters out fluctuations with wavelengths much shorter than the NV–sample distance h .

For conducting samples, the relevant degrees of freedom are fluctuating currents $\mathbf{J}(\mathbf{r}, t)$, which produce magnetic fields via the Biot–Savart law. The fluctuation–dissipation theorem links current noise to the conductivity tensor $\sigma_{\alpha\beta}(\mathbf{q}, \omega)$:

$$S_{J_\alpha J_\beta}(\mathbf{q}, \omega) \propto \frac{2\hbar}{1 - e^{-\hbar\omega/k_B T}} \omega \text{Re} \sigma_{\alpha\beta}(\mathbf{q}, \omega). \quad (15)$$

In the classical, low-frequency limit, this reduces to Johnson–Nyquist noise proportional to $k_B T \sigma$ [2, 13]. Analytic expressions for $S_B(\omega)$ at height h above a conducting half-space (Fig. 2b) or thin film are available and have been used to interpret Johnson-noise relaxometry data [13, 16]. These expressions show, for example, how Γ_1 scales with T , σ , and h , and how finite thickness or skin depth modify the simple half-space picture [13].

For superconductors, the situation is more subtle: Meissner screening and vortices reorganize currents in a way that can both suppress and enhance field noise at the NV location, depending on temperature, field, and geometry [19, 63]. Here, again, the conceptual structure is the same: one computes the spectrum of current or vortex fluctuations, propagates them to the NV position via appropriate Green’s functions, and identifies the transverse component at ω_{NV} .

In all these cases, the message is that geometry and distance matter as much as the intrinsic material response. Two materials with the same $\chi''(\omega)$ or $\sigma(\omega)$ can produce very different $S_B(\omega)$ at the NV if the sensor is at different distances or if the sample geometry is different (e.g., a strip vs. an infinite film). Careful modeling of the propagator—or at least robust scaling tests vs. h and geometry—is therefore essential for quantitative relaxometry [1, 2, 13, 14].

4.5 Cross-relaxometry: resonant coupling as spectroscopy

Cross-relaxometry arises when the NV transition frequency comes into resonance with a transition of nearby target spins or modes. Let ω_{NV} be the NV transition frequency and ω_t be the target frequency (which may

depend on B). When the detuning

$$\Delta(B) = \omega_{\text{NV}}(B) - \omega_{\text{t}}(B) \quad (16)$$

passes through zero, energy-conserving flip-flop processes become efficient, enhancing the NV relaxation rate [9, 10].

A simple model considers a single NV coupled to a single spin-1/2 via a dipolar interaction with transverse coupling strength J . In the interaction picture and rotating-wave approximation, the effective Hamiltonian for the flip-flop subspace can be written as

$$\mathcal{H}_{\text{int}} = \frac{\hbar\Delta}{2}(\sigma_z^{\text{NV}} - \sigma_z^{\text{t}}) + \hbar J(\sigma_+^{\text{NV}}\sigma_-^{\text{t}} + \sigma_-^{\text{NV}}\sigma_+^{\text{t}}), \quad (17)$$

where “t” denotes the target spin and Δ the detuning. Coupling to an environment (phonons, other spins, motion) gives the target spin a finite correlation time τ_c , which leads to a Lorentzian-like spectral density centered at ω_{t} with width $\sim 1/\tau_c$ [9, 11].

Within a Bloch–Redfield picture, the NV relaxation rate due to this resonant process can be approximated as

$$\Gamma_{1,\text{CR}}(B) \sim \frac{J^2\tau_c}{1 + \Delta^2(B)\tau_c^2}, \quad (18)$$

i.e., a Lorentzian in B (or in frequency) centered at the cross-relaxation condition $\Delta(B) = 0$. More realistic models for ensembles of target spins or magnons replace J^2 and τ_c with effective parameters that incorporate distributions of positions, couplings, and local fields, but the qualitative picture—a resonance in $\Gamma_1(B)$ —remains [9, 12].

Two regimes are particularly important in practice. In electron-spin cross-relaxation, target transitions lie in the MHz–GHz range (e.g., paramagnetic defects, radicals, transition-metal ions). By sweeping B and recording $T_1(B)$, one obtains an electron-spin resonance spectrum with contrast proportional to the density and coupling of the target spins [9, 12]. In nuclear-spin cross-relaxation near the ground-state level anticrossing (GSLAC), at $B_{\parallel} \sim 102$ mT the $m_s = 0$ and $m_s = -1$ levels approach degeneracy and hybridize with nearby nuclear spins, reducing ω_{NV} into the MHz range. This allows overlap with nuclear Larmor frequencies and enables microwave-free nano-NMR: features in $T_1(B)$ reveal nuclear species and their couplings to the NV [10, 11, 23, 24].

Cross-relaxation spectra can be broadened or shifted by static disorder (e.g., inhomogeneous fields in powders), diffusion and motion (in liquids), and strong coupling between the NV and target. Extracting quantitative information from line shapes therefore typically requires at least a minimal model of the target spin environment and its dynamics [10–12]. Nevertheless, even qualitatively, the presence or absence of particular cross-relaxation features as a function of B is a powerful fingerprint of the spin species and modes present in the sample, making cross-relaxometry a central tool in NV-based spectroscopy and nano/micro-NMR [9–12, 15, 23, 24].

5. EXPERIMENTAL APPLICATIONS OF SPIN RELAXOMETRY

5.1 Condensed matter systems

5.1.1 Conductors

In regular conductors, the magnetic noise in the system is dominated by fluctuations arises from the thermal excited current, commonly described as Johnson-Nyquist noise. The stochastic thermal currents produce broadband magnetic fields that encompass the transition frequencies between $|m_s = 0\rangle$ and $|m_s = \pm 1\rangle$ states, thereby driving spin relaxation [13, 16].

In 2015, Kolkowitz *et al.* employed shallow NV spins to detect thermally induced magnetic field fluctuations originating from proximal silver films [13]. By depositing a layer of SiO_2 between the diamond surface and silver film with a gradually increasing thickness, they measured the variations in the longitudinal spin relaxation rate Γ_1 with the NV-sample separation distance d (Fig. 3a). Combining with the temperature control, they reached a model where the relaxation rate scales with the conductivity σ of the metal and inverse distance as $\Gamma_1 \propto T\sigma/d$. This work established NV relaxometry as a non-invasive probe capable of measuring local electron transport without the need for electrical contacts.

Subsequent studies extended this technique to non-equilibrium transport dynamics in two-dimensional materials. Andersen *et al.* (2019) utilized shallow NV centers to probe the local magnetic noise generated by high-mobility graphene devices driven into the non-linear transport regime [64]. By mapping the NV spin relaxation rate along the conduction channel, the authors revealed a spatial asymmetry in the current fluctuations that was inaccessible via global transport measurements. The local noise was found to grow exponentially along the direction of carrier drift, with the spatial profile inverting upon reversal of the current or charge carrier sign (Fig. 3b). These results demonstrate the unique capability of solid-state defects to image the buildup of collective excitations in mesoscopic systems.

5.1.2 Ferromagnets and Antiferromagnets

The application of NV relaxometry to magnetically ordered systems has diverged into two main streams: imaging spin textures that do not generate net stray field, and probing the critical dynamics near magnetic phase transitions.

Imaging Antiferromagnetic Textures — The spin textures such as domain walls, spin spirals, and skyrmions in antiferromagnets are notoriously difficult to image using conventional methods due to their vanishing net magnetization. While these textures may not generate a static

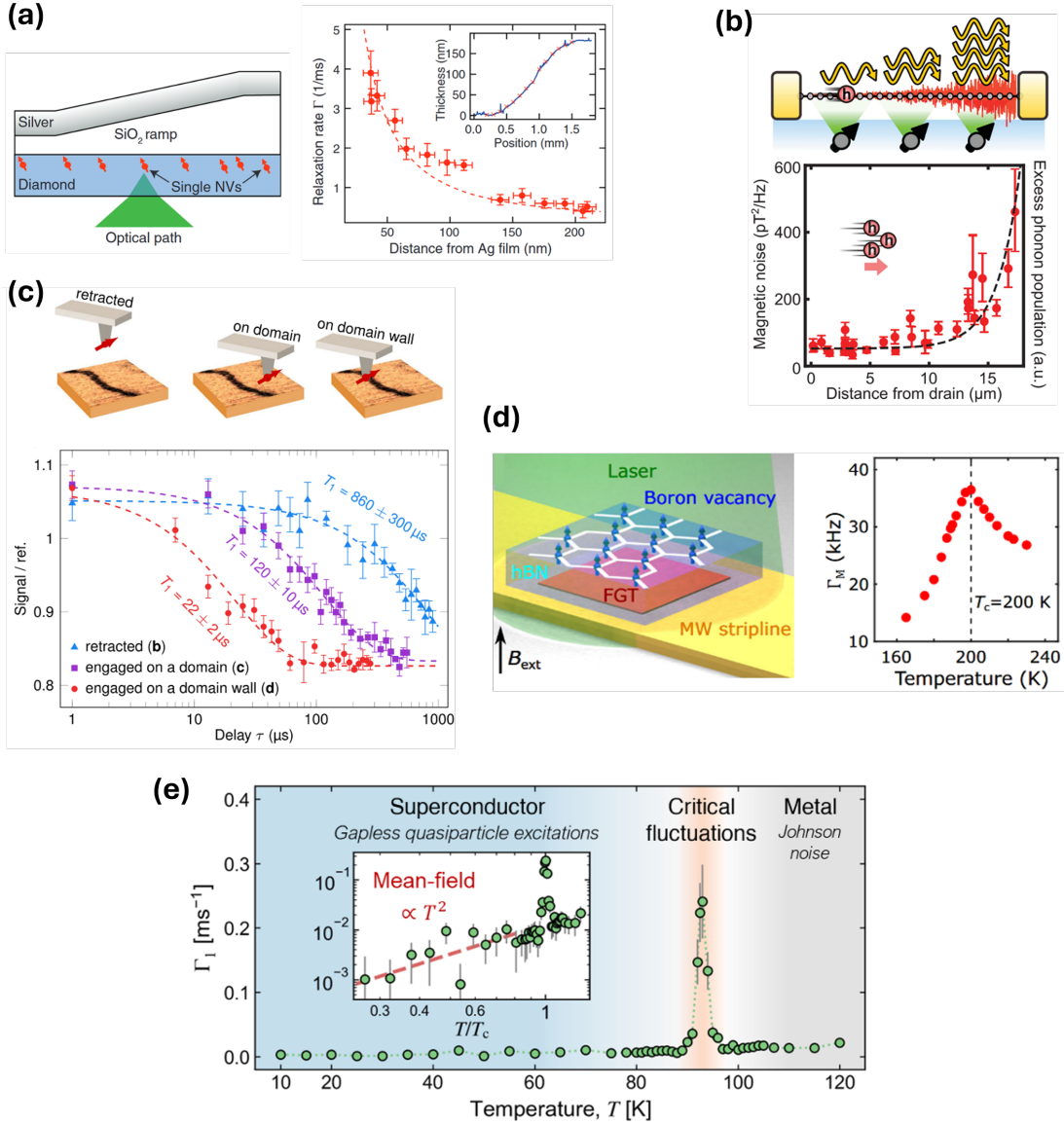


FIG. 3. Experimental applications in condensed matter systems. (a) Probing Johnson noise in metal using single NV centers. A layer of SiO₂ is grown on the diamond surface with gradually increasing thickness, followed by a 60 nm silver film. The NV relaxation rate Γ_1 is measured as a function of distance from the silver film, scaling inversely with distance. Adapted from Ref. [13]. (b) Investigating non-equilibrium dynamics in graphene. A hBN-encapsulated graphene device on diamond substrate (upper panel). The local magnetic noise, probed by the NV relaxation rate, is measured as a function of distance from the drain, consistent with the exponential growth of phonons (lower panel). Adapted from Ref. [64]. (c) Imaging domain walls in a synthetic antiferromagnet. The relaxation time T_1 of the NV center decreases dramatically when engaged on a domain wall, compared to on domain or retracted. Adapted from Ref. [17]. (d) Imaging the spin fluctuations in a van der Waals ferromagnet with boron vacancy centers in hBN. A Fe₃GeTe₂(FGT)/hBN van der Waals heterostructure is transferred on a gold microwave stripline (left panel). The temperature-dependent relaxation rate exhibits a peak amplitude at the phase transition temperature $T_c = 200$ K (right panel). Adapted from Ref. [46]. (e) Probing superconducting dynamics in a thin film Bi₂Sr₂CaCu₂O_{8+ δ} (BSCCO). The relaxation rate Γ_1 of NV on BSCCO is measured as a function of temperature. In the absence of magnetic field, it reveals three distinct regimes: Johnson noise in metallic phase, nodal quasiparticles excitations deep in superconducting phase, and critical fluctuations near the phase transition. Adapted from Ref. [19].

magnetic field, they are sites of localized spin dynamics, which couples to NV relaxation. In 2021, Finco *et al.* demonstrated an all-optical imaging mode using single NV center where the relaxation rate is mapped by record-

ing the photoluminescence (PL) intensity under continuous laser illumination [17]. At domain walls, a significantly enhanced spin relaxation is observed. In contrast, at uniform antiferromagnetic domain region, less spin

noise was detected due to the spin wave gap (Fig. 3c). This work established relaxometry as a versatile tool for mapping materials where static stray fields are negligible.

Probing Phase Transitions — Near a continuous magnetic phase transition, such as the Curie temperature (T_c) of a ferromagnet or the Néel temperature (T_n) of an antiferromagnet, the correlation length of spin fluctuations diverges, manifesting as a dramatic increase in magnetic noise [65].

Recent studies have utilized relaxometry to map the phase transition of various magnetic materials with nanoscale precision, especially in 2D van der Waals magnets [46, 66, 67]. For instance, Huang *et al.* (2022) demonstrated nanoscale imaging of low-dimensional ferromagnetism in $\text{Fe}_3\text{GeTe}_2/\text{hBN}$ van der Waals heterostructures [46]. By performing wide-field spin relaxometry on boron-vacancy centers in hBN, they observed a distinct peak in the relaxation rate around the Curie temperature (Fig. 3d). This enhancement was attributed to the critical divergence of the longitudinal magnetic susceptibility near the phase transition. These experiments highlight the capability of solid-state spins to act as local probes of criticality.

5.1.3 Superconductors

Superconductors represent a macroscopic quantum state of matter defined by zero electrical resistance and the perfect expulsion of magnetic fields. While solid-state defects, such as NV centers, have been primarily employed to study the static magnetic features including Meissner effect and vortices induced by applied magnetic fields [], recent advances have moved beyond static imaging to probing the dynamics of the superconducting condensate and its excitations via relaxometry.

The first experimental demonstration of this technique was achieved in a high- T_c superconductor $\text{Bi}_2\text{Sr}_2\text{CaCu}_2\text{O}_{8+\delta}$ (BSCCO) [19]. By transferring an exfoliated BSCCO flake onto the diamond surface hosting a shallow layer of NV centers, Liu *et al.* (2025) utilized relaxometry to map distinct dynamical regimes across different phases. At low temperatures ($T \ll T_c$), the authors identified a $\Gamma_1 \propto T^2$ power-law dependence, providing direct evidence for nodal quasiparticle excitations characteristic of d -wave pairing. Approaching the critical temperature T_c , the relaxation rate exhibited a sharp divergence attributed to critical fluctuations of the superconducting order parameter (Fig. 3e). Furthermore, under applied magnetic fields, the additional noise induced by diffusive motion of the vortex liquid exhibit a clear linear dependence on the applied field strength, enabling the quantitative extraction of vortex diffusivity. These results establish quantum relaxometry as a versatile platform for resolving complex dynamical phenomena in correlated materials.

5.2 Biological Applications

A central goal in bio-sensing is quantitative, localized readout of physiologically relevant variables (ions, radicals, biomolecules, pH, temperature, and etc.) inside living systems. Conventional modalities often face trade-offs among sensitivity, selectivity, invasiveness, and resolution, and many cannot access the microscopical process in single living cells under physiological conditions [].

Solid state defect, with NV centers in particular, are attractive because they combine optical addressability at room temperature with excellent bio-compatibility from their chemical inertness. The most popular platform for studying biological processes is nanodiamond/fluorescent nanodiamond (FND) for straightforward integration with biological systems. FNDs can be easily dispersed in liquids, surface-functionalized, and internalized by cells. At the same time, it can be also implemented with other modalities including scanning NV [68], wide-field NV layers, and etc. with varying spatial resolution, photon collection, and sample compatibility.

For a broader perspective on diamond NV-based biosensing beyond relaxometry, the reader is referred to recent reviews of quantum sensors for biomedical applications and focused reviews on fluorescent nanodiamond/NV biosensing platforms [69–71]. Here we narrow the discussion to relaxometry-driven biological readouts.

Many biological important signals are carried by unpaired electron spins, including radicals, transition-metal ions, and spin labels. In these settings, T_1 relaxometry is particularly useful because fluctuating electron spins generate transverse magnetic noise that shortens T_1 . Relaxometry in cells focuses mapping the spin-fluctuation-driven changes in T_1 to infer concentrations of dynamics of paramagnetic species, including free radicals and paramagnetic ions.

Since the 2022 review by Schirhagl *et al.* [1], the field has matured from detecting static concentrations of paramagnetic ions in buffer to resolving spatiotemporal dynamics in living systems. The recent literature is characterized by a shift toward mapping non-equilibrium “radical dialogues” in host-pathogen interactions, quantifying magnetic phase transitions in metalloproteins, and validating alternative host materials like silicon carbide (SiC) for physiological compatibility. Figure 4 displays a summary of NV spin relaxometry used in bioscience.

5.2.1 Intracellular Radical Dynamics and Metabolic Profiling

The primary biological application of nanodiamond (ND) relaxometry remains the detection of reactive oxygen species (ROS), but recent work has moved beyond binary “stress detection” to resolve complex signaling timelines.

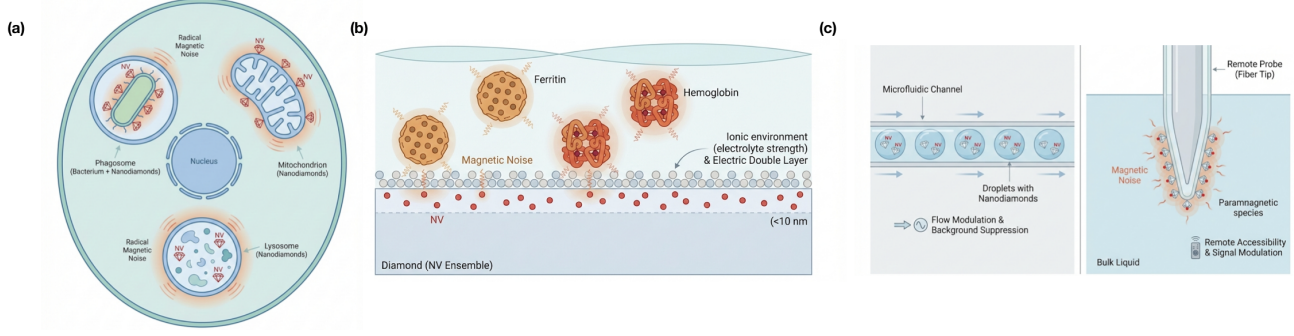


FIG. 4. Experimental applications in biological systems. (a) Intracellular radical dynamics. Targeted fluorescent nanodiamonds enable nanoscale T_1 relaxometry inside living cells, allowing spatially and temporally resolved readout of radical-driven spin noise at specific intracellular locations, including bacterial surfaces, mitochondria, and lysosomes. (b) Chip-scale biomolecular assays. Planar diamond substrates with shallow near-surface NV ensembles provide quantitative relaxometry of paramagnetic biomolecules in controlled assay environments. (c) Integrated and scalable platforms. Microfluidic and fiber-integrated relaxometry platforms address throughput and accessibility by enabling signal modulation, background suppression, and remote sensing in complex biological fluids.

Mapping the "Radical Dialogue" in Infection. A persistent challenge in immunology is distinguishing between the host's oxidative attack and the pathogen's antioxidative defense. In 2023, Wu et al. utilized fluorescent nanodiamonds (FNDs) conjugated directly to the surface of *Staphylococcus aureus* to probe this interaction inside macrophages [72]. Relaxometry measurements revealed a biphasic response: an initial T_1 reduction corresponding to the macrophage oxidative burst, followed by a recovery of T_1 specifically at the bacterial surface starting 80 minutes post-infection. This provided the first direct, nanoscale evidence of the pathogen actively scavenging radicals to evade immune clearance, a localized survival mechanism invisible to bulk ROS assays.

Organelle-Specific Metabolic Footprinting. Targeted sensing has revealed that delivery vectors themselves alter metabolic states, a confound often overlooked in standard toxicity assays. Wu et al. (2024) demonstrated that the mitochondrial targeting ligand Triphenylphosphonium (TPP) inherently downregulates intracellular radical production, whereas the signaling peptide Somatostatin (SST) upregulates it [73]. Similarly, Fan et al. (2024) applied antibody-targeted FNDs to track real-time mitochondrial radical bursts in keratinocytes during UVB exposure [74]. These studies highlight the necessity of controlling for the "oxidative footprint" of the sensor's own targeting moiety to avoid misinterpretation of metabolic data.

Mechanistic Chemistry In Situ. Relaxometry has also been applied to elucidate intracellular reaction mechanisms. Lu et al. (2024) coated NDs with a thin layer of eumelanin—a pigment with complex radical chemistry—and internalized them into lysosomes [75]. The T_1 response quantified the formation of semiquinone radicals via a comproportionation reaction, which was found to be strictly pH-dependent. By correlating the radical

count with theoretical models, the sensors acted as transducers, mapping the lysosomal pH via the radical proxy.

5.2.2 Chip-Scale Interfaces and Biomolecular Assays

Planar diamond substrates with shallow NV ensembles (<10 nm depth) have matured into quantitative platforms for analyzing metalloproteins, though recent physical insights demand updated calibration protocols. Freire-Moschovitis et al. (2023) overturned the assumption that physiological salts primarily add magnetic noise; they found that diamagnetic electrolytes actually increase T_1 by stabilizing surface charge states via electric double layer formation [76]. This "diamagnetic effect" requires that bio-assays rigorously control ionic strength to avoid artifacts. In applications, Grant et al. (2023) utilized relaxometry for "magnetic phasemetry" of ferritin, revealing a nonmonotonic noise scaling that signifies a structural transition from disordered iron clusters to a crystalline core [77]. Clinically, Lamichhane et al. (2024) demonstrated the quantification of methemoglobin in <100 pL volumes, establishing a linear response curve suitable for rapid, micro-scale blood analysis [78].

5.2.3 Integrated Platforms: Microfluidics and Fibers

To address the low throughput of single-particle tracking, engineering efforts have focused on integrating quantum sensors with scalable fluidics. Sarkar et al. (2024) introduced a "double lock-in" scheme by encapsulating nanodiamonds in flowing picoliter droplets [79]. The periodic flow modulates the fluorescence signal, suppressing low-frequency background noise to levels comparable

with bulk crystals and enabling high-throughput single-cell screening. For remote sensing, Cheng *et al.* (2024) developed an all-fiber probe with nanodiamonds chemically anchored to a tapered tip [80]. This "dip-stick" geometry successfully detected pH changes and specific biomarkers in bulk fluids where optical access is otherwise restricted.

5.2.4 Emerging Materials and In Vivo Translation

While diamond remains the gold standard, we have seen significant milestones in alternative host materials and whole-organism imaging.

Bridging the gap to multicellular organisms, Fan *et al.* (2025) reported the first *in vivo* relaxometry mapping of oxidative stress in a *Caenorhabditis elegans* model of Huntington's disease [81]. By microinjecting FNDs into specific tissues, they detected a statistically significant elevation of free radicals in body wall muscles expressing PolyQ aggregates compared to the intestine, directly linking protein aggregation to localized oxidative stress in a living animal.

Silicon carbide has emerged as a novel platform for biological applications due to its biocompatibility and industrial maturity. Li *et al.* (2025) demonstrated stable, room-temperature divacancy qubits in alkene-terminated SiC that function as bioinert sensors [53]. Crucially, SiC defects emit in the near-infrared (NIR), offering superior tissue penetration compared to the visible emission of NV centers. Parallelly, hexagonal Boron Nitride (hBN) is being explored for its 2D nature, which allows defects to be atomically close to the target. Robertson *et al.* (2023) utilized hBN powder to detect paramagnetic Gd^{3+} ions, proving that van der Waals materials can bring the sensor-target separation to the angstrom scale, maximizing dipolar coupling [82].

5.2.5 Outlook and bottlenecks

Across reviews, the main bottlenecks are consistent: improving sensitivity and temporal resolution for dynamic measurements in biological environments, enabling programmable targeting to specific intracellular locations, and mitigating cross-talk among simultaneously varying parameters.

5.3 Spin Dynamics: Cross-Relaxation, Diamond Surface, and Nuclear Spins

5.3.1 Cross-relaxation spectroscopy

Cross-relaxation (CR) spectroscopy can be understood as a field-tunable, frequency-selective T_1 measurement:

the NV longitudinal relaxation rate $\Gamma_1 \equiv 1/T_1$ samples the transverse magnetic-noise spectral density near the NV transition frequency ω_{NV} (see Sec. 4.5 for theory). Sweeping the bias field B_0 tunes $\omega_{\text{NV}}(B_0)$ and converts spectral features in the environment into a characteristic field dependence $\Gamma_1(B_0)$. When ω_{NV} approaches a discrete bath resonance, dipolar-mediated exchange is enhanced and produces sharp signatures in Γ_1 (dips in T_1) whose linewidths are set by the effective broadenings of the NV and bath transitions [83].

A canonical benchmark is the NV-P1 "standard candle." Hall *et al.* demonstrated T_1 -based electron spin resonance (ESR) spectroscopy by tuning an NV ensemble through the NV-P1 resonance near $B_0 \approx 512$ G and observing a pronounced reduction of T_1 , then using the field dependence to reconstruct the hyperfine-resolved ESR spectrum of the substitutional-nitrogen (P1) bath [83]. Beyond its pedagogical value, this result established a practical workflow that recurs across modern CR experiments: (i) identify resonance fields where Γ_1 is enhanced, (ii) fit the dip features to obtain resonance positions and linewidths, and (iii) map those features back to bath transition frequencies and couplings.

CR features are also a useful handle in dense, interacting spin environments where multiple sub-ensembles coexist. For example, P1-resolved relaxation signatures have been leveraged to separate frequency-selected channels within strongly interacting dipolar baths, allowing NV depolarization dynamics to report on which bath subgroups participate in resonant exchange [84]. Systematic ensemble measurements further clarified how these channels compete with phonons: Jarmola *et al.* mapped T_1 versus field and temperature and showed that sample-dependent cross-relaxation processes (including NV-NV and NV-P1 channels) can dominate low-temperature relaxation when phonon-assisted pathways are suppressed [85]. Complementary concentration-dependent studies established that increasing defect densities strengthens and broadens CR resonances, making $\Gamma_1(B_0)$ line shapes a quantitative diagnostic of paramagnetic-impurity density and disorder in NV ensembles [86].

Two practical features make CR relaxometry attractive for applications. First, it is naturally sensitive to fast-fluctuating electron-spin targets whose noise power resides in the GHz band, and it can be deployed as a wide-band spectroscopy tool by tuning ω_{NV} over a large frequency range via B_0 [9, 83]. Second, spectral selectivity continues to improve as experiments and models better disentangle overlapping impurity signatures and microwave-driven artifacts in optically detected CR observables [87].

An important extension of CR physics appears near the NV ground-state level anticrossing (GSLAC) at $B_0 \approx 1024$ G, where electron-nuclear mixing reshapes the relevant splittings and enables purely optical access to low-frequency magnetic noise. Broadway *et al.* showed

that, in this regime, microwave-free protocols can detect magnetic-noise components from the MHz scale down toward the sub-MHz range, opening an all-optical route to CR-like sensitivity in a band that overlaps nuclear Larmor frequencies at modest fields [88].

Finally, CR relaxometry is increasingly used as a *readout layer* for optically “dark” spins in heterogeneous materials. Recent scanning-NV work demonstrated ESR detection of boron-vacancy defects (V_B^-) in hBN by monitoring changes in the NV T_1 while tuning the NV transition through the NV- V_B^- cross-relaxation condition, thereby avoiding any requirement for direct fluorescence-based readout of the target defect [89]. This hybrid 2D/3D strategy highlights a broader theme: once the NV is established as a calibrated relaxometric transducer, CR spectroscopy can be extended to material platforms where conventional optical or inductive ESR is impractical. Moreover, the scanning geometry enables sub-diffraction-limited, spatially resolved mapping of defect populations, providing a quantitative route to imaging defect density variations across heterogeneous 2D landscapes (Fig. 5a).

5.3.2 Surface spin noise and charge dynamics in shallow-NV relaxometry

Shallow NV centers (typically $\lesssim 10$ nm below the diamond interface) are essential for nanoscale relaxometry because the signal from external targets rises rapidly as the NV is brought closer to the sample. In practice, the same proximity exposes the NV to a second, unavoidable “target”: magnetic and electric-field fluctuations associated with the diamond surface. These surface-induced fluctuations can dominate both T_1 and T_2 , setting a sensitivity floor that must be quantified and engineered around.

Multiple experiments show that relaxation and dephasing accelerate sharply as the NV approaches the surface, consistent with a surface-localized noise source rather than a bulk mechanism. Rosskopf *et al.* measured T_1 , $T_{1\rho}$, and T_2 for very shallow NV centers (depth ~ 5 nm) and observed relaxation-time reductions of up to $\sim 30\times$ relative to bulk, consistent with ubiquitous surface-associated magnetic impurities [5]. Their analysis supports a dilute but consequential surface spin density (reported as ~ 0.01 to $0.1 \mu_B/\text{nm}^2$) and fast surface-spin dynamics with a characteristic correlation time $\tau_c \approx 0.28$ ns. In a complementary approach, Myers *et al.* used depth-calibrated NVs and dynamical decoupling to isolate surface-driven dephasing, with results consistent with a surface bath of electronic spins and a correlation rate on the order of 200 kHz in the spectral window relevant to dephasing [90]. These two studies are consistent in the key applied message: the dominant noise is localized near the interface, and it is dynamical

rather than purely static.

A practical point for relaxometry is that “the correlation time” extracted from an NV experiment depends on the frequency band being interrogated. Rosskopf *et al.* reported sub-nanosecond dynamics compatible with a broadband magnetic spectrum that can efficiently relax the NV at its transition frequency [5]. Romach *et al.* further emphasized that shallow NVs experience a structured spectrum: their analysis supports a double-Lorentzian form with a low-frequency component consistent with a surface electronic spin bath and an additional faster component attributed to surface-modified phononic coupling [6]. For applied work, this implies that improving T_2 does not automatically guarantee improved T_1 , and vice versa. Both must be measured in the operating regime of the intended sensing protocol.

Attempts to reduce surface noise have shown that chemical termination alone is not the full story; surface morphology controls whether a termination is reproducible and stable. Sangtawesin *et al.* combined surface spectroscopy with single-NV measurements and demonstrated that a highly ordered, oxygen-terminated surface can suppress noise (Fig. 5b), with shallow NV centers (within 10 nm) exhibiting coherence times extended by about an order of magnitude [7]. In parallel, Stacey *et al.* provided evidence that diamond surfaces can host sp^2 -related defects that act as electron traps and plausible noise sources, reinforcing the view that near-surface disorder and reconstruction can produce persistent electronic states even after standard processing [91]. Taken together, the working consensus is that the surface hosts electronic defect states whose spin and charge dynamics both matter, and whose mitigation requires controlling both chemical termination and near-surface structure.

Measurement artifact: charge conversion can mimic fast T_1 . Near-surface NVs often exhibit charge-state instabilities that directly impact relaxometry readout. Bluvstein *et al.* showed that shallow NVs can display surface-dependent charge dynamics, including ionization on experimentally relevant timescales, which can degrade ODMR contrast and complicate spin-based measurements [92]. For T_1 relaxometry in particular, Barbosa *et al.* quantified how laser-driven conversion between NV^- and NV^0 can distort the apparent relaxation: charge conversion occurs even below saturation, and at higher excitation intensities it can dominate the measured fluorescence decay, producing an artificially short “ T_1 ” if not accounted for [93]. In applied measurements, it is therefore essential to (i) operate at low enough optical power to suppress charge conversion, (ii) normalize fluorescence appropriately, and (iii) whenever possible, utilize differential measurement or monitor NV^0 emission in parallel to disentangle spin relaxation from charge dynamics [86, 93–96].

For nanoscale relaxometry with shallow NVs, surface noise is best treated as an engineered baseline rather

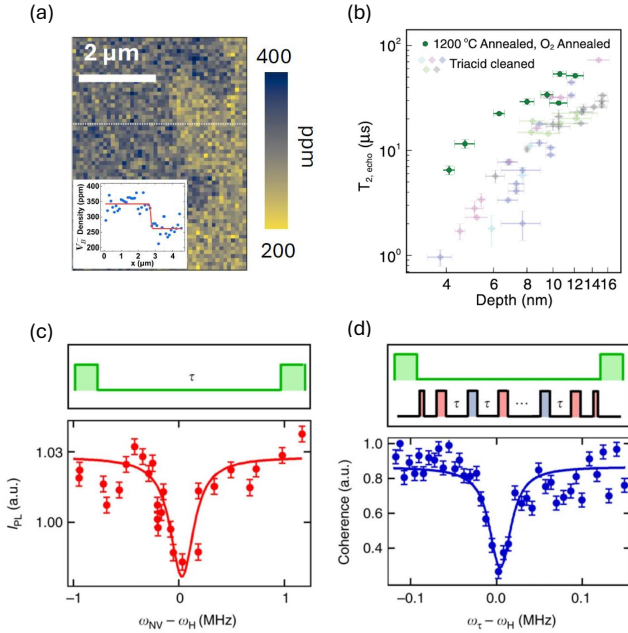


FIG. 5. Experimental applications in spin dynamics. (a) Defect density map of boron vacancies obtained using scanning NV cross-relaxometry. Inset: The profile of V_B^- density as a function of position, over the line indicated by the white dashed line. Adapted from Ref. [89]. (b) Comparison of Hahn echo coherence times ($T_{2,\text{echo}}$) as a function of NV depth. The high-temperature and oxygen-annealed sample (colored markers) exhibits significantly improved coherence times at the same depths compared to those under a standard triacid-cleaned surface (grey markers). Adapted from Ref. [7]. (c)-(d) Representative spectra from poly(methyl methacrylate) (PMMA) measured with a single ^{14}NV center using (c) microwave-free T_1 relaxometry and (d) an XY8-N dynamical-decoupling sequence ($N=256$ microwave π -pulses). The corresponding pulse sequences are shown schematically, with laser pulses in green and microwave pulses in red (0° phase) or blue (90° phase). Adapted from Ref. [10].

than a nuisance. Three practical guidelines recur across the literature: (i) quantify the baseline by measuring both T_1 and T_2 (and their power dependence) on the same device and surface condition [5, 90]; (ii) stabilize the surface by controlling morphology and termination, with ordered oxygen termination as a demonstrated route to substantially improved shallow-NV coherence [7]; (iii) treat charge stability as part of the sensing protocol by choosing excitation conditions and analysis workflows that explicitly separate charge conversion from spin relaxation [92, 93]. These constraints define the operating envelope in which relaxometry on external targets can be interpreted quantitatively.

5.3.3 Nanoscale NMR and Nuclear Spin Dynamics

NV-detected nanoscale NMR turns a near-surface nitrogen-vacancy (NV) center into a local magnetic spectrometer for nuclear spins within a few nanometers of the diamond surface. Early ambient-condition demonstrations detected statistically polarized proton ensembles by converting nuclear Larmor precession into an AC magnetic signal and filtering it with dynamical-decoupling sequences [97, 98]. A key point is that, at the nanoscale, the measured signal is often not the thermal mean magnetization but the root-mean-square spin fluctuations: for N spins, the effective polarization scales as \sqrt{N} , so even $N \sim 10^4$ nuclei can produce a detectable fluctuating moment [99, 100]. This statistical-polarization regime enables spectroscopy from nanometer-scale detection volumes under room-temperature conditions.

Beyond identifying nuclear species via their Larmor frequencies, NV-based nano-NMR can access *dynamics*. Correlation-type measurements reveal temporal structure in the nuclear field, which encodes molecular motion and local relaxation processes in the near-surface environment [101]. This capability is practically important because nuclear diffusion and surface-driven spectral wandering are often the dominant linewidth mechanisms in liquids near the diamond surface, and they set the performance ceiling for chemical analysis at the nanoscale [101].

Historically, NV-based NMR spectroscopy has been dominated by dynamical-decoupling readout (e.g., XY8), which interrogates nuclear precession through coherent control and therefore requires microwave instrumentation and nontrivial pulse sequences. A useful counterpoint is that NMR spectra can also be accessed in a purely relaxometric modality, with the NV serving as a field-tunable spectral filter for nuclear spin noise. A particularly instructive example is the microwave-free nano-NMR scheme of Wood *et al.* [10]. In that work, a shallow NV center is placed under a nanoscale organic layer rich in proton spins, and the bias field is tuned close to the NV ground-state level anti-crossing so that the NV transition frequency enters the MHz regime and becomes resonant with the ^1H Larmor frequency. Under these conditions, cross-relaxation between the NV and the external nuclear spins enhances the NV longitudinal relaxation rate whenever $\omega_{\text{NV}}(B)$ matches the proton resonance, so that a sweep of B directly yields an NMR spectrum encoded in $T_1(B)$. Crucially, neither the NV nor the nuclear spins are driven by microwaves; the only control is static field tuning and optical initialization/readout. Wood *et al.* showed that this simplified, all-optical protocol achieves a sensitivity comparable to more complex microwave-pulse-based nano-NMR schemes, while probing a $\sim (10 \text{ nm})^3$ volume of external proton spins under ambient conditions [10]. This experiment illustrates that

NV T_1 relaxometry, combined with field-tunable cross-relaxation, can reveal nanoscale NMR spectra in a minimally invasive and experimentally compact fashion. The spectral resolution in T_1 -based NMR is ultimately limited by the effective linewidth of the resonant transitions, which in many practical cases is set by the dephasing rate $1/T_2^*$ (i.e., inhomogeneous broadening). Consequently, the achievable resolution can be poorer than that of coherent, phase-accumulation NV-NMR protocols, where dynamical decoupling enables frequency resolution approaching $1/T_2$ (Fig. 5c-d).

The same principle can, in principle, be extended from point spectroscopy to *spatially resolved* nuclear-spin imaging: by combining field-tuned T_1 relaxometry with either scanning-probe geometry or wide-field NV ensembles, one can construct maps of $T_1(B, \mathbf{r})$ in which NMR contrast is encoded in the relaxation rate. Such T_1 -based nano-/micro-NMR complements phase-based NV NMR protocols: relaxometry naturally probes nuclear-spin *fluctuations* via cross-relaxation, while coherent NV-NMR schemes probe phase accumulation under controlled RF pulse sequences. Together, these techniques provide a unified route to nuclear-spin spectroscopy in which T_1 relaxometry supplies a simple, all-optical readout channel with field-tunable spectral selectivity.

In summary, *relaxometry-based* nuclear-spin spectroscopy with NV centers leverages field-tunable cross-relaxation to encode NMR contrast directly in the longitudinal relaxation rate. By sweeping B to tune $\omega_{\text{NV}}(B)$ across nuclear resonances, one obtains an NMR spectrum as features in $T_1(B)$, without relying on phase-accumulation protocols. Compared with coherent NV-NMR schemes, T_1 -based NMR is experimentally compact, naturally sensitive to stochastic nuclear fluctuations, and readily compatible with scanning and wide-field implementations. More broadly, relaxometry provides a unified framework spanning spin species and frequency scales, connecting nuclear-spin spectroscopy via cross-relaxation to GHz-band sensing of electronic and magnonic noise in quantum materials.

6. CONCLUSION AND OUTLOOK

NV spin relaxometry has evolved from a niche technique into a general-purpose nanoscale noise-spectroscopy platform. Its strength lies in turning complex dynamics into an experimentally accessible decay rate while retaining a quantitative link to the underlying magnetic-noise power spectral density. The method is now established across condensed matter (magnons, antiferromagnets, transport noise), spectroscopy (cross-relaxometry and relaxometry-based NMR), and bio/chem sensing (radicals and metal ions), with increasing reach into new host materials and device settings.

Looking forward, a central scientific opportunity is to move from *contrast* to *inference*: from imaging “where noise is” to extracting *what noise is* in terms of microscopic mechanisms and material parameters. In practice this means estimating not only a local rate map $\Gamma_1(\mathbf{r})$, but the underlying spectral and spatial structure of fluctuations—e.g., $S_{B\perp}(\omega)$ and, when relevant, the associated response functions such as $\chi''(\mathbf{q}, \omega)$ or $\sigma(\mathbf{q}, \omega)$. Achieving this will require measurement sets that deliberately span multiple spectral windows and geometric filters: combining T_1 , $T_{1\rho}$, and coherence-based probes (T_2 , dynamical decoupling) across multiple bias fields and multiple sensor–sample distances (depth series, scanning height sweeps, or engineered spacer layers). The payoff is a form of “noise tomography” that can disentangle competing channels (surface spins vs. sample excitations; magnetic vs. electric noise; Johnson noise vs. magnetic order-parameter fluctuations) and enable quantitative comparisons to theory and simulation.

A second near-term accelerator is *throughput*. Wide-field cameras already provide parallel relaxometry, but the next step is to make relaxometry fast enough for statistically rich datasets (device variability, spatial heterogeneity, kinetics) and for feedback-based experiments (adaptive field sweeps, real-time mapping during switching, heating, or reaction progress). Promising directions include improved optical readout (spin-to-charge conversion, repetitive readout, and optimized collection optics), lock-in style protocols for suppressing technical drifts, and compressed-sensing / adaptive sampling strategies that target the most informative field points in $\Gamma_1(B)$ rather than uniformly scanning. For scanning geometries, advances in probe stability, drift correction, and real-time height control will be as important as raw sensitivity, because quantitative inversion hinges on reliable knowledge of the sensor–sample distance. For wide-field implementations, recent advances in single-photon avalanche diode (SPAD) array cameras—especially time-gated architectures with nanosecond-scale temporal resolution—can substantially reduce the acquisition time for T_1 -based imaging [102].

A third frontier is *integration with extreme or device-relevant environments*. Cryogenic relaxometry can access superconducting quasiparticles, vortex dynamics, and correlated excitations whose noise spectra are sharply temperature and field dependent. At the same time, high-field operation and improved field stability broaden spectral coverage and sharpen cross-relaxation features, enabling more selective spectroscopy (and potentially relaxometry-based microscale NMR in compact geometries). More generally, integrating relaxometry with functioning devices—2D heterostructures under bias, nanoelectronic channels, magnetic tunnel junctions, superconducting circuits, and gated van der Waals magnets—positions relaxometry as a local probe of *nonequilibrium* fluctuations, where the noise itself carries infor-

mation about dissipation pathways and emergent collective modes.

The *materials landscape* will also broaden. Diamond NV remains the benchmark, but 2D and device-compatible hosts offer complementary advantages: defects in hBN provide intrinsically small standoff and heterostructure compatibility, while SiC offers wafer-scale processing and near-IR emission that is attractive for integrated photonics and bio-adjacent use cases. A practical theme across hosts is that relaxometry performance is often limited by *interfaces* rather than bulk: surface paramagnetism, charge traps, adsorbate dynamics, and electric-field noise can dominate shallow sensors. Thus, progress in surface science (termination control, reconstruction suppression, ultrathin encapsulation layers, and reproducible cleaning/processing) is likely to translate directly into improved relaxometric sensitivity and interpretability.

An additional and increasingly important advantage of spin relaxometry emerges in *high magnetic-field and high-frequency regimes*, where conventional coherent-control techniques become impractical. At bias fields exceeding ~ 1 T, the NV ESR frequency exceeds ~ 30 GHz, rendering the delivery of resonant microwave pulses for Rabi driving or dynamical decoupling technically challenging due to the lack of efficient sources, transmission losses, and sample heating. In this regime, standard ODMR- and pulse-based protocols effectively break down. In contrast, all-optical spin relaxometry remains fully operational: the longitudinal relaxation rate continues to sensitively probe magnetic noise from the thermal or driven bath without requiring any resonant RF control, making relaxometry a high-dynamic-range sensing modality that is naturally compatible with extreme fields and frequencies. This capability is particularly relevant for studying high-frequency collective excitations such as antiferromagnetic magnons, whose characteristic frequencies in thin-film systems often span tens to hundreds of gigahertz and are difficult to access using conventional RF-based antiferromagnetic resonance techniques. By applying a strong magnetic field aligned with the sensor's quantization axis, the ESR frequency of the spin defect can be tuned into resonance with these magnon modes, enabling their detection via cross-relaxation once magnons are excited thermally, electrically, or phononically. More broadly, the ability to operate without applied RF fields makes relaxometry uniquely suited to environments where RF delivery is infeasible or undesirable, including cryogenic platforms, nanoscale devices, and biological or soft-matter systems where RF-induced heating or perturbation must be minimized.

In life-science and chemistry, the most compelling directions go beyond “detecting radicals” toward *quantitative, targeted, time-resolved readouts* in complex environments. This includes mapping spatiotemporal radical dynamics during immune response and infection, moni-

toring redox-active pathways in organelles, and building microfluidic or droplet platforms for higher-throughput assays where relaxometry becomes a screening tool rather than a bespoke measurement. Key enablers will be improved targeting chemistries, calibration strategies that remain valid in heterogeneous ionic environments, and protocols that minimize phototoxicity and local heating. A realistic long-term target is multiplexed relaxometry, where several analytes or microenvironments are discriminated by combining spectral selectivity (field tuning / rotating-frame windows) with engineered spin labels or binding motifs.

Across all applications, several challenges must be addressed for relaxometry to become a broadly quantitative metrology tool. Surface and charge stability remain central: shallow sensors face surface-spin noise and charge conversion that can masquerade as fast T_1 or distort apparent contrast, so robust operating envelopes require power-dependent controls, charge-state monitoring, and improved surface preparation/encapsulation. Quantitative inversion and identifiability are equally important: mapping $\Gamma_1(h, B, T)$ back to a unique $S(\omega)$ (or to material parameters) is often ill-posed, and progress will rely on multi-contrast datasets, physically constrained models, and principled uncertainty quantification to avoid over-interpreting non-unique fits. Geometry and distance calibration can be a dominant error source because near-field kernels strongly weight spatial wavelengths and decay rapidly with standoff, so small uncertainties in NV depth or scan height can translate into large errors in inferred parameters. Field, temperature, and drift control are also critical: cross-relaxometry and GSLAC-adjacent nuclear spectroscopy demand stable bias fields and careful management of laser-induced heating and drift, especially in long acquisitions or cryogenic setups. Finally, standardization and benchmarking will be essential—community-wide reference samples, shared analysis pipelines, and standardized reporting (including confidence intervals and control measurements) are needed to compare results across platforms and to build reliable “noise libraries” for common materials and surfaces.

In summary, the next phase of NV (and related defect) relaxometry will be defined less by whether a signal can be detected and more by whether it can be *interpreted* and *used*—to extract microscopic dynamics, to diagnose and optimize quantum/mesoscopic devices *in situ*, and to enable quantitative bio/chemical assays at previously inaccessible length scales. As theory, simulation, and instrumentation co-design mature, relaxometry is poised to become a standard tool for studying dynamical phenomena in quantum materials, nanoelectronics, and living systems.

ACKNOWLEDGMENTS

This work was supported by the Center for Nanophase Materials Sciences, (CNMS), which is a US Department of Energy, Office of Science User Facility at Oak Ridge National Laboratory. H.Z. and A.M. were supported by the Laboratory Directed Research and Development Program of Oak Ridge National Laboratory, managed by UT-Battelle, LLC, for the U.S. Department of Energy. R.G., G.H., Z.L. and C.Z. acknowledge support from the NSF under Grant No. 2514391.

AUTHOR DECLARATIONS

Conflict of Interest: The authors have no conflicts to disclose.

Author Contributions: Ruotian Gong, Alex L. Melendez, Guanghui He, and Zhongyuan Liu contributed equally to this paper.

* zu@wustl.edu; Corresponding author.

† zhaoh1@ornl.gov; Corresponding author.

- [1] A. Mzyk, A. Sigaeva, and R. Schirhagl, Accounts of chemical research **55**, 3572 (2022).
- [2] C. L. Degen, F. Reinhard, and P. Cappellaro, Reviews of modern physics **89**, 035002 (2017).
- [3] J. Tetienne, T. Hingant, and L. Rondin, Physical Review B **87**, 235436 (2013).
- [4] J. F. Barry, J. M. Schloss, E. Bauch, M. J. Turner, C. A. Hart, L. M. Pham, and R. L. Walsworth, Reviews of Modern Physics **92**, 015004 (2020).
- [5] T. Rosskopf, A. Dussaux, K. Ohashi, M. Loretz, R. Schirhagl, H. Watanabe, S. Shikata, K. M. Itoh, and C. Degen, Physical review letters **112**, 147602 (2014).
- [6] Y. Romach, C. Müller, T. Unden, L. J. Rogers, T. Isoda, K. M. Itoh, M. Markham, A. Stacey, J. Meijer, S. Pezzagna, B. Naydenov, L. P. McGuinness, N. Bar-Gill, and F. Jelezko, Phys. Rev. Lett. **114**, 017601 (2015).
- [7] S. Sangtawesin, B. L. Dwyer, S. Srinivasan, J. J. Allred, L. V. H. Rodgers, K. De Greve, A. Stacey, N. Dotschuk, K. M. O'Donnell, D. Hu, D. A. Evans, C. Jaye, D. A. Fischer, M. L. Markham, D. J. Twitchen, H. Park, M. D. Lukin, and N. P. de Leon, Phys. Rev. X **9**, 031052 (2019).
- [8] I. Cardoso Barbosa, J. Gutsche, and A. Widera, Physical Review B **108**, 075411 (2023).
- [9] J. D. A. Wood, D. A. Broadway, L. T. Hall, A. Stacey, D. A. Simpson, J.-P. Tetienne, and L. C. L. Hollenberg, Phys. Rev. B **94**, 155402 (2016).
- [10] J. D. Wood, J.-P. Tetienne, D. A. Broadway, L. T. Hall, D. A. Simpson, A. Stacey, and L. C. Hollenberg, Nature communications **8**, 15950 (2017).
- [11] D. A. Broadway, J.-P. Tetienne, A. Stacey, J. D. Wood, D. A. Simpson, L. T. Hall, and L. C. Hollenberg, Nature communications **9**, 1246 (2018).
- [12] C. Mignon, A. R. Ortiz Moreno, H. Shirzad, S. K. Padamati, V. G. Damle, Y. Ong, R. Schirhagl, and M. Chipaux, ACS sensors **8**, 1667 (2023).
- [13] S. Kolkowitz, A. Safira, A. High, R. Devlin, S. Choi, Q. Unterreithmeier, D. Patterson, A. Zibrov, V. Manucharyan, H. Park, *et al.*, Science **347**, 1129 (2015).
- [14] B. A. McCullian, A. M. Thabt, B. A. Gray, A. L. Melendez, M. S. Wolf, V. L. Safonov, D. V. Pelekhover, V. P. Bhalla, M. R. Page, and P. C. Hammel, Nature communications **11**, 5229 (2020).
- [15] S. Takei and Y. Tserkovnyak, Physical Review Research **6**, 013043 (2024).
- [16] A. Ariyaratne, D. Bluvstein, B. A. Myers, and A. C. B. Jayich, Nature communications **9**, 2406 (2018).
- [17] A. Finco, A. Haykal, R. Tanos, F. Fabre, S. Chouaieb, W. Akhtar, I. Robert-Philip, W. Legrand, F. Ajejas, K. Bouzehouane, *et al.*, Nature communications **12**, 767 (2021).
- [18] B. G. Simon, S. Kurdi, H. La, I. Bertelli, J. J. Carmiggelt, M. Ruf, N. De Jong, H. Van Den Berg, A. J. Katan, and T. Van Der Sar, Nano Letters **21**, 8213 (2021).
- [19] Z. Liu, R. Gong, J. Kim, O. K. Diessel, Q. Xu, Z. Rehfuss, X. Du, G. He, A. Singh, Y. S. Eo, *et al.*, arXiv preprint arXiv:2502.04439 (2025).
- [20] M. W. Doherty, N. B. Manson, P. Delaney, F. Jelezko, J. Wrachtrup, and L. C. Hollenberg, Physics Reports **528**, 1 (2013).
- [21] L. Rondin, J.-P. Tetienne, T. Hingant, J.-F. Roch, P. Maletinsky, and V. Jacques, Reports on progress in physics **77**, 056503 (2014).
- [22] R. Schirhagl, K. Chang, M. Loretz, and C. L. Degen, Annual review of physical chemistry **65**, 83 (2014).
- [23] R. D. Allert, K. D. Briegel, and D. B. Bucher, Chemical Communications **58**, 8165 (2022).
- [24] J. Du, F. Shi, X. Kong, F. Jelezko, and J. Wrachtrup, Reviews of Modern Physics **96**, 025001 (2024).
- [25] S. Steinert, F. Ziem, L. Hall, A. Zappe, M. Schweikert, N. Götz, A. Aird, G. Balasubramanian, L. Hollenberg, and J. Wrachtrup, Nature communications **4**, 1607 (2013).
- [26] P. Maletinsky, S. Hong, M. S. Grinolds, B. Hausmann, M. D. Lukin, R. L. Walsworth, M. Loncar, and A. Yacoby, Nature nanotechnology **7**, 320 (2012).
- [27] E. V. Levine, M. J. Turner, P. Kehayias, C. A. Hart, N. Langellier, R. Trubko, D. R. Glenn, R. R. Fu, and R. L. Walsworth, Nanophotonics **8**, 1945 (2019).
- [28] J. J. Hamlin and B. B. Zhou, Science **366**, 1312 (2019).
- [29] S. Hsieh, P. Bhattacharyya, C. Zu, T. Mittiga, T. Smart, F. Machado, B. Kobrin, T. Höhn, N. Rui, M. Kamrani, *et al.*, Science **366**, 1349 (2019).
- [30] P. Bhattacharyya, W. Chen, X. Huang, S. Chatterjee, B. Huang, B. Kobrin, Y. Lyu, T. Smart, M. Block, E. Wang, *et al.*, Nature **627**, 73 (2024).
- [31] M. Lesik, T. Plisson, L. Toraille, J. Renaud, F. Occelli, M. Schmidt, O. Salord, A. Delobbe, T. Debuisschert, L. Rondin, *et al.*, Science **366**, 1359 (2019).
- [32] K. Y. Yip, K. O. Ho, K. Y. Yu, Y. Chen, W. Zhang, S. Kasahara, Y. Mizukami, T. Shibauchi, Y. Matsuda, S. K. Goh, *et al.*, Science **366**, 1355 (2019).
- [33] F. Perona Martínez, A. C. Nusantara, M. Chipaux, S. K. Padamati, and R. Schirhagl, ACS sensors **5**, 3862 (2020).

[34] S. Vaidya, X. Gao, S. Dikshit, I. Aharonovich, and T. Li, *Advances in Physics: X* **8**, 2206049 (2023).

[35] A. Gottscholl, M. Kianinia, V. Soltamov, S. Orlinskii, G. Mamin, C. Bradac, C. Kasper, K. Krambrock, A. Sperlich, M. Toth, *et al.*, *Nature materials* **19**, 540 (2020).

[36] A. Gottscholl, M. Diez, V. Soltamov, C. Kasper, A. Sperlich, M. Kianinia, C. Bradac, I. Aharonovich, and V. Dyakonov, *Science Advances* **7**, eabf3630 (2021).

[37] R. Gong, G. He, X. Gao, P. Ju, Z. Liu, B. Ye, E. A. Henriksen, T. Li, and C. Zu, *Nature Communications* **14**, 3299 (2023).

[38] R. Gong, X. Du, E. Janzen, V. Liu, Z. Liu, G. He, B. Ye, T. Li, N. Y. Yao, J. H. Edgar, *et al.*, *Nature communications* **15**, 104 (2024).

[39] Z. Liu, R. Gong, B. Huang, Y. Jin, X. Du, G. He, E. Janzen, L. Yang, E. A. Henriksen, J. H. Edgar, *et al.*, *Physical Review B* **111**, 024108 (2025).

[40] S. Biswas, G. Scuri, N. Huffman, E. I. Rosenthal, R. Gong, T. Poirier, X. Gao, S. Vaidya, A. J. Stein, T. Weissman, *et al.*, *arXiv preprint arXiv:2509.08984* (2025).

[41] H. L. Stern, Q. Gu, J. Jarman, S. Eizagirre Barker, N. Mendelson, D. Chugh, S. Schott, H. H. Tan, H. Sirringhaus, I. Aharonovich, *et al.*, *Nature communications* **13**, 618 (2022).

[42] H. L. Stern, C. M. Gilardoni, Q. Gu, S. Eizagirre Barker, O. F. Powell, X. Deng, S. A. Fraser, L. Follet, C. Li, A. J. Ramsay, *et al.*, *Nature Materials* **23**, 1379 (2024).

[43] N. Chejanovsky, A. Mukherjee, J. Geng, Y.-C. Chen, Y. Kim, A. Denisenko, A. Finkler, T. Taniguchi, K. Watanabe, D. B. R. Dasari, *et al.*, *Nature materials* **20**, 1079 (2021).

[44] N. Mendelson, D. Chugh, J. R. Reimers, T. S. Cheng, A. Gottscholl, H. Long, C. J. Mellor, A. Zettl, V. Dyakonov, P. H. Beton, *et al.*, *Nature materials* **20**, 321 (2021).

[45] X. Gao, S. Vaidya, P. Ju, S. Dikshit, K. Shen, Y. P. Chen, and T. Li, *ACS Photonics* **10**, 2894 (2023).

[46] M. Huang, J. Zhou, D. Chen, H. Lu, N. J. McLaughlin, S. Li, M. Alghamdi, D. Djugba, J. Shi, H. Wang, *et al.*, *Nature communications* **13**, 5369 (2022).

[47] J. Zhou, H. Lu, D. Chen, M. Huang, G. Q. Yan, F. Al-Matouq, J. Chang, D. Djugba, Z. Jiang, H. Wang, *et al.*, *Science Advances* **10**, eadk8495 (2024).

[48] M. Widmann, S.-Y. Lee, T. Rendler, N. T. Son, H. Federer, S. Paik, L.-P. Yang, N. Zhao, S. Yang, I. Booker, *et al.*, *Nature materials* **14**, 164 (2015).

[49] G. Wolfowicz, C. P. Anderson, A. L. Yeats, S. J. Whiteley, J. Niklas, O. G. Poluektov, F. J. Heremans, and D. D. Awschalom, *Nature communications* **8**, 1876 (2017).

[50] R. Nagy, M. Niethammer, M. Widmann, Y.-C. Chen, P. Udvarhelyi, C. Bonato, J. U. Hassan, R. Karhu, I. G. Ivanov, N. T. Son, *et al.*, *Nature communications* **10**, 1954 (2019).

[51] D. J. Christle, P. V. Klimov, C. F. de las Casas, K. Szász, V. Ivády, V. Jokubavicius, J. Ul Hassan, M. Syväjärvi, W. F. Koehl, T. Ohshima, *et al.*, *Physical Review X* **7**, 021046 (2017).

[52] H. Seo, A. L. Falk, P. V. Klimov, K. C. Miao, G. Galli, and D. D. Awschalom, *Nature communications* **7**, 12935 (2016).

[53] P. Li, J.-Y. Zhou, S. Li, P. Udvarhelyi, J.-S. Xu, C.-F. Li, B. Huang, G.-C. Guo, and A. Gali, *Nature Materials* **1**, 1 (2025).

[54] C. W. Thiel, T. Böttger, and R. Cone, *Journal of luminescence* **131**, 353 (2011).

[55] S. Bertaina, S. Gambarelli, A. Tkachuk, I. Kurkin, B. Malkin, A. Stepanov, and B. Barbara, *Nature nanotechnology* **2**, 39 (2007).

[56] P. Siyushev, K. Xia, R. Reuter, M. Jamali, N. Zhao, N. Yang, C. Duan, N. Kukharchyk, A. Wieck, R. Kolesov, *et al.*, *Nature communications* **5**, 3895 (2014).

[57] H. Zhao, S. M. Hus, J. Chen, X. Yan, B. J. Lawrie, S. Jesse, A.-P. Li, L. Liang, and H. Htoon, *ACS nano* **19**, 6911 (2025).

[58] H. Zhao, M. T. Pettes, Y. Zheng, and H. Htoon, *Nature communications* **12**, 6753 (2021).

[59] J. Chen, C. Cui, B. Lawrie, Y. Xue, S. Guha, M. Eichenfield, H. Zhao, and X. Yan, *Nanophotonics* **14**, 1687 (2025).

[60] J.-Y. Tsai, J. Pan, H. Lin, A. Bansil, and Q. Yan, *Nature communications* **13**, 492 (2022).

[61] L. Shang, Q. Chen, W. Jing, C.-G. Ma, C.-K. Duan, and J. Du, *Physical Review Materials* **6**, 086201 (2022).

[62] Y. Lee, Y. Hu, X. Lang, D. Kim, K. Li, Y. Ping, K.-M. C. Fu, and K. Cho, *Nature Communications* **13**, 7501 (2022).

[63] S. P. Kelly and Y. Tserkovnyak, *arXiv preprint arXiv:2412.05465* (2024).

[64] T. I. Andersen, B. L. Dwyer, J. D. Sanchez-Yamagishi, J. F. Rodriguez-Nieva, K. Agarwal, K. Watanabe, T. Taniguchi, E. A. Demler, P. Kim, H. Park, *et al.*, *Science* **364**, 154 (2019).

[65] Y. Li, Z. Ding, C. Wang, H. Sun, Z. Chen, P. Wang, Y. Wang, M. Gong, H. Zeng, F. Shi, and J. Du, *Nature Communications* **16**, 8585 (2025).

[66] M. E. Ziffer, F. Machado, B. Ursprung, A. Lozovoi, A. B. Tazi, Z. Yuan, M. E. Ziebel, T. Delord, N. Zeng, E. Telford, *et al.*, *arXiv preprint arXiv:2407.05614* (2024).

[67] Y.-C. Wu, G. B. Halász, J. T. Damron, Z. Gai, H. Zhao, Y. Sun, K. A. Dahmen, C. Sohn, E. W. Carlson, C. Hua, *et al.*, *Nano letters* **25**, 1473 (2025).

[68] P. Wang, S. Chen, M. Guo, S. Peng, M. Wang, M. Chen, W. Ma, R. Zhang, J. Su, X. Rong, *et al.*, *Science advances* **5**, eaau8038 (2019).

[69] N. Aslam, H. Zhou, E. K. Urbach, M. J. Turner, R. L. Walsworth, M. D. Lukin, and H. Park, *Nature Reviews Physics* **5**, 157 (2023).

[70] T. Zhang, G. Pramanik, K. Zhang, M. Gulka, L. Wang, J. Jing, F. Xu, Z. Li, Q. Wei, P. Cigler, *et al.*, *ACS sensors* **6**, 2077 (2021).

[71] Y. Wu and T. Weil, *Advanced Science* **9**, 2200059 (2022).

[72] K. Wu, L. Nie, A. C. Nusantara, W. Woudstra, T. Vede-laar, A. Sigaeva, and R. Schirhagl, *ACS nano* **17**, 1100 (2023).

[73] K. Wu, Q. Lu, M. Sow, P. Balasubramanian, F. Jelezko, T. Weil, and Y. Wu, *Functional Diamond* **4**, 2336524 (2024).

[74] S. Fan, L. Lopez Llorens, F. P. Perona Martinez, and R. Schirhagl, *ACS sensors* **9**, 2440 (2024).

[75] Q. Lu, B. Vosberg, Z. Wang, P. Balasubramanian, M. Sow, C. Volkert, R. Gonzalez Brouwer, I. Lieber-

wirth, R. Graf, F. Jelezko, *et al.*, Journal of the American Chemical Society **146**, 7222 (2024).

[76] F. A. Freire-Moschovitis, R. Rizzato, A. Pershin, M. R. Schepp, R. D. Allert, L. M. Todenhagen, M. S. Brandt, A. Gali, and D. B. Bucher, ACS nano **17**, 10474 (2023).

[77] E. S. Grant, L. T. Hall, L. C. Hollenberg, G. McColl, and D. A. Simpson, ACS nano **17**, 372 (2022).

[78] S. Lamichhane, E. C. Guevara, I. Fescenko, S.-H. Liou, R. Y. Lai, and A. Laraoui, Applied Physics Letters **125** (2024).

[79] A. Sarkar, Z. R. Jones, M. Parashar, E. Druga, A. Akkiraju, S. Conti, P. Krishnamoorthi, S. Nachuri, P. Aman, M. Hashemi, *et al.*, Science Advances **10**, eadp4033 (2024).

[80] H. Cheng, Y. Luo, X. Luo, C. Xue, Y. Li, G. Liu, L. Chen, Z. Chen, and Y. Chen, Optics Express **32**, 29265 (2024).

[81] S. Fan, Y. Zhang, A. P. Ainslie, R. Seinstra, T. Zhang, E. Nollen, and R. Schirhagl, Advanced Science **12**, 2412300 (2025).

[82] I. O. Robertson, S. C. Scholten, P. Singh, A. J. Healey, F. Meneses, P. Reineck, H. Abe, T. Ohshima, M. Kianinia, I. Aharonovich, *et al.*, ACS nano **17**, 13408 (2023).

[83] L. Hall, P. Kehayias, D. Simpson, A. Jarmola, A. Stacey, D. Budker, and L. Hollenberg, Nature communications **7**, 10211 (2016).

[84] C. Zu, F. Machado, B. Ye, S. Choi, B. Kobrin, T. Mittiga, S. Hsieh, P. Bhattacharyya, M. Markham, D. Twitchen, *et al.*, Nature **597**, 45 (2021).

[85] A. Jarmola, V. Acosta, K. Jensen, S. Chemerisov, and D. Budker, Physical review letters **108**, 197601 (2012).

[86] M. Mrózek, D. Rudnicki, P. Kehayias, A. Jarmola, D. Budker, and W. Gawlik, EPJ Quantum Technology **2**, 22 (2015).

[87] R. Lazda, L. Busaite, A. Berzins, J. Smits, F. Gahbauer, M. Auzinsh, D. Budker, and R. Ferber, Physical Review B **103**, 134104 (2021).

[88] D. A. Broadway, J. D. Wood, L. T. Hall, A. Stacey, M. Markham, D. A. Simpson, J.-P. Tetienne, and L. C. Hollenberg, Physical Review Applied **6**, 064001 (2016).

[89] A. L. Melendez, R. Gong, G. He, Y. Wang, Y.-C. Wu, T. Poirier, S. Randolph, S. Ghosh, L. Liang, S. Jesse, A.-P. Li, J. T. Damron, B. J. Lawrie, J. H. Edgar, I. V. Vlassiouk, C. Zu, and H. Zhao, Nanoscale quantum imaging of spin dynamics using a hybrid 2d/3d system (2025), arXiv:2504.09432 [cond-mat.mtrl-sci].

[90] B. A. Myers, A. Das, M. C. Dartailh, K. Ohno, D. D. Awschalom, and A. C. Bleszynski Jayich, Phys. Rev. Lett. **113**, 027602 (2014).

[91] A. Stacey, N. Dotschuk, J.-P. Chou, D. A. Broadway, A. K. Schenk, M. J. Sear, J.-P. Tetienne, A. Hoffman, S. Prawer, C. I. Pakes, A. Tadich, N. P. de Leon, A. Gali, and L. C. L. Hollenberg, Advanced Materials Interfaces **6**, 1801449 (2019).

[92] D. Bluvstein, Z. Zhang, and A. C. Bleszynski Jayich, Phys. Rev. Lett. **122**, 076101 (2019).

[93] I. Cardoso Barbosa, J. Gutsche, and A. Widera, Phys. Rev. B **108**, 075411 (2023).

[94] J. Choi, S. Choi, G. Kucsko, P. C. Maurer, B. J. Shields, H. Sumiya, S. Onoda, J. Isoya, E. Demler, F. Jelezko, *et al.*, Physical review letters **118**, 093601 (2017).

[95] G. He, B. Ye, R. Gong, Z. Liu, K. W. Murch, N. Y. Yao, and C. Zu, Physical Review Letters **131**, 130401 (2023).

[96] G. He, B. Ye, R. Gong, C. Yao, Z. Liu, K. W. Murch, N. Y. Yao, and C. Zu, Physical Review X **15**, 011055 (2025).

[97] H. J. Mamin *et al.*, Science **339**, 557 (2013).

[98] T. Staudacher *et al.*, Science **339**, 561 (2013).

[99] C. A. Meriles *et al.*, The Journal of Chemical Physics **133**, 124105 (2010).

[100] B. Herzog, D. Cadeddu, F. Xue, P. Peddibhotia, and M. Poggio, Applied Physics Letters **105**, 043112 (2014).

[101] T. Staudacher, N. Raatz, S. Pezzagna, J. Meijer, F. Reinhard, C. A. Meriles, and J. Wrachtrup, Nature Communications **6**, 8527 (2015).

[102] C. Bruschini and E. Charbon, Reporters, Markers, Dyes, Nanoparticles, and Molecular Probes for Biomedical Applications XV **12862**, 22 (2024).